

A Frequency-Modulated Tripedal Soft Magnetic Robot With Diverse Motion Modalities for Ingestible Applications

Ruijie Tang[✉] and Hongliang Ren[✉], *Senior Member, IEEE*

Abstract—Soft robots driven by the external magnetic field can be widely applied in medical areas to realize noninvasive diagnosis and treatment. These robots gain advantages in flexibility, untethered remote control, and safe human interaction. Thus, they can achieve functions such as endo-imaging, drug delivery, and biopsy. However, developing a multi-functional magnetic-driven soft robot to carry out various medical missions remains challenging. In this work, we design a tripedal soft magnetic robot with three radial-magnetized cylindric permanent magnets embedded in three soles. The diverse motion modalities as the prerequisites to realize multifunctionality are explored in this work. The motion generation of the devised robot is investigated by applying an external uniform magnetic field. The motion modalities for movement include butterfly crawling (along the x and y axis), scorpion crawling, and rolling. We develop the different control signals from a three-directional magnetic field in various shapes, frequencies, amplitudes, and offsets for our tripedal soft magnetic robot. At different frequencies, the robot exhibits different behaviors in terms of speed and trajectory under different moving modalities. The motion trajectory of the robot in its designated direction shows a wave-like upward trend. The maximum velocity of the butterfly crawling and scorpion crawling motion at the frequency of 1 Hz is measured to be 5.30 mm/s and 9.06 mm/s. The robot can overcome obstacles such as polyps and wrinkles using the scorpion crawling and rolling mechanisms. Aiming at the potential medical application such as biopsy, we designed the leg raising modality ranging from a low frequency to a high frequency (0.02 Hz, 0.1 Hz, 0.5 Hz) using different control signal profiles (step, cosine, inverse exponential).

Index Terms—Medical robots and systems, soft robot applications, soft robot materials and design.

Manuscript received 22 September 2023; accepted 26 December 2023. Date of publication 18 January 2024; date of current version 25 January 2024. This letter was recommended for publication by Associate Editor S. Song and Editor Y.-L. Park upon evaluation of the reviewers' comments. This work was supported in part by Hong Kong Research Grants Council (RGC) Collaborative Research Fund under Grants CRF C4026-21GF and CRF C4063-18G, in part by General Research Fund under GRF Grant 14216022, in part by NSFC/RGC Joint Research Scheme N_CUHK420/22, in part by Shenzhen-Hong Kong-Macau Technology Research Programme (Type C) under Grant 202108233000303, and in part by Guangdong Basic and Applied Basic Research Foundation (GBABF) under Grant 2021B1515120035. (*Corresponding author: Hongliang Ren.*)

Ruijie Tang is with the Department of Electronic Engineering, The Chinese University of Hong Kong, Hong Kong SAR, China (e-mail: 1155171824@link.cuhk.edu.hk).

Hongliang Ren is with the Department of Electronic Engineering, The Chinese University of Hong Kong, Hong Kong SAR, China, and also with the Department of Electronic Engineering Shun Hing Institute of Advanced Engineering, The Chinese University of Hong Kong, Hong Kong SAR, China (e-mail: hlren@ieee.org).

This letter has supplementary downloadable material available at <https://doi.org/10.1109/LRA.2024.3355783>, provided by the authors.

Digital Object Identifier 10.1109/LRA.2024.3355783

I. INTRODUCTION

DIGESTIVE system diseases are a prevalent category of illnesses that can severely affect patients' quality of life. The implementation of robotic technology in the medical field offers new opportunities for treating these diseases. Robots can execute intricate surgical procedures with precision and flexibility, enhancing the safety and success rate of operations. However, these robots resemble continuous systems like gastroscopes or colonoscopes, which can still cause discomfort for patients, and the treatment process has not been significantly simplified. Therefore, some researchers have proposed and designed a series of small, untethered robots for targeted delivery and therapy in the digestive system [1].

Two common propulsion methods for small robots are self-propulsion [2], [3] and magnetic actuation [4]. Magnetically actuated robots, powered by external permanent magnets or coils, can perform a variety of movements and even walk within the body by utilizing magnetic field gradients or magnetic torque. Firstly, robot configurations can be categorized into film type, capsule type, ped type, and origami type. Each of these configurations has its own strengths and weaknesses and specific application scenarios for which they are best suited. Inspired by cilia, Gu [5] et al. proposed programmable magnetization patterns embedded in cilia carpets to be transported in the amphibious environment. The film-type robot's most significant advantage is its ability to generate various forms of locomotion, with up to 7 modalities being discovered [6]. It has also been successfully demonstrated to move on an ex-vivo swine stomach. By installing micro-spines at both ends of the film, a robot with the same structure can achieve the functions of surface adhesion and climbing [7]. This design allows the robot to effectively navigate and maneuver on various surfaces within the body. In this letter [8], despite using the term "multi-leg," the robot should still be classified as a film-type overall. This is because its multiple legs can be considered as a form of magnetic encoding on the film. The film-type magnetic robots show advantages in precise control tasks such as leader-follower, path following, and position control in [8], [9], [10]. However, the payload of film type is limited by its materials and structure. For the capsule type [11], [12], [13], [14], the movement mode is based on rolling, and it can be regarded as a permanent magnet when modeling and analyzing, so there will be no difficulty moving in the environment. The applicable scenarios also include basic

functions such as biopsy and endoscopy for the treatment and detection of gastrointestinal diseases. In addition, the RoboCap robot [15] designed by Srinivasan et al. can also be used for mucus removal and drug delivery through an additional cutting device. However, the absence of sophisticated locomotion techniques presents a challenge for capsule-type micro-robots in executing tasks that demand high levels of precision.

Furthermore, ped-type micro magnetic drive robots are capable of exhibiting a diverse range of motion modalities and functional designs. The controllable four-legged robots, as demonstrated in [16] and [17], can surmount obstacles and perform tasks such as grasping, transporting, and puncturing. In [18], a robot, resembling the form of a jellyfish, has been proposed and utilized for the purpose of drug transportation. Through the development of intricate foot configurations and programmable magnetization techniques, robots have been engineered to exhibit capabilities such as jumping, rolling, crawling, and reconfigurability [19], [20]. The final type of robot to be discussed is the origami magnetic robot [21], [22], [23]. This robot is characterized by its intricate mechanical structure, which enables it to execute unanticipated movements and its relative ease of fabrication. Nevertheless, a notable limitation is its susceptibility to interference and restricted functionality within the gastrointestinal tract.

For the purpose of discussion, the digestive system can be divided into three sections: the esophagus, stomach, and intestine. The esophagus is characterized by its elongated and linear terrain, with a full-of-air environment. The primary challenge for robot locomotion within this region is to overcome the resistance imposed by fluids and the strong adhesion experienced underwater. Within the stomach, the terrain is considerably more complex, featuring numerous wrinkled surfaces and a thick mucus layer. As such, robots operating within this environment must possess the ability to navigate through high-viscosity and obstacle-laden conditions, while also contending with gastric peristalsis. Additionally, due to the acidic nature of the stomach environment, with a pH ranging from 1-4, it is imperative that the robot's material composition exhibits acid-resistant properties. The intestine is distinguished by its length and the presence of a mucus layer. Consequently, robots must also demonstrate proficiency in traversing viscous environments and overcoming intestinal peristalsis.

Practical applications in the digestive system require robots with high precision and robustness. Therefore, we chose the ped-type soft magnetic robot as the design basis, due to its multi-locomotion and relatively high payload. In Fig. 1, the robot is expected to move in the GI tract (purple arrow), such as the stomach, by changing different moving modalities when encountering different terrain. When the robot reaches the lesion area, two functional modalities are used to perform a biopsy (legs raising modality) or to stir the mucus (legs shaking).

In this work, We have developed a tripedal soft magnetic drive robot, specifically designed for use within the digestive tract. The dimensions of the robot have been carefully calibrated to facilitate movement and the execution of relevant tasks within the confines of the digestive tract. The objective of the work is to address the motion modalities generated by magnetic fields

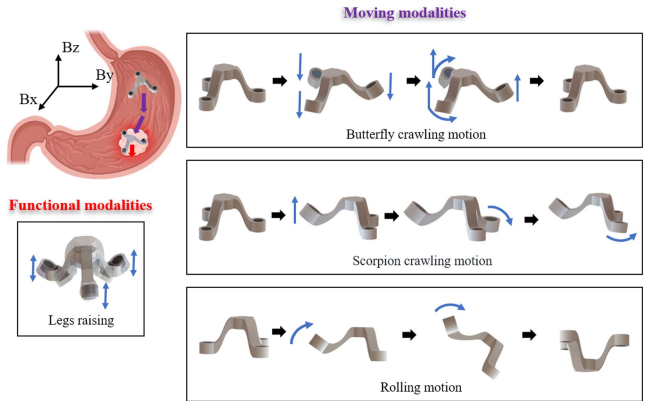


Fig. 1. Soft magnetic robot is actuated by 3D magnetic field. The robot is designed with three moving modalities (butterfly crawling motion, scorpion crawling motion, and rolling motion) and one functional modality (legs raising).

with frequency modulation. The *key contributions* of this letter are as follows:

- 1) We have devised and analyzed three distinct modes of locomotion, comprising two crawling movements that emulate the motions of butterfly swimming and scorpion crawling, as well as a rolling motion designed to surmount particularly challenging obstacles.
- 2) By modulating the frequency in the range of 0.1-1 Hz, the maximum speeds achieved for butterfly crawling motion and scorpion crawling motion were found to be 5.30 mm/s and 9.06 mm/s. The related normalized velocities (body length per second) are 0.22 and 0.38.
- 3) To facilitate the vertical motion evaluation, we have conducted a thorough analysis and evaluation of three distinct external magnetic field signals. Our findings indicate that a sinusoidal signal is capable of achieving optimal stability at an average peak force variance of 0.15, while an inverse exponential signal is able to generate the maximum force at 21.6 mN.

II. FABRICATION AND DESIGN OF SOFT MAGNETIC ROBOT

Our design concept for this robot follows the fundamental framework from requirements to parameters. The first step involves identifying the clinical requirements for gastrointestinal applications, specifically the ability to navigate through irregular terrains and accomplish the task of microneedle insertion. In the second step, considering these requirements, we design motion modalities that satisfy clinical needs. We determined that the robot's motion modes should include rolling, crawling, and upward thrusting as fundamental modalities. In the literature review mentioned earlier, it was noted that film-type, ped-type, and origami-type robots all have the potential for the mentioned motion modes. As for the tripedal design, a triangular structure is the minimum structure capable of forming stability. Besides, the tripodal configuration is the minimum number of legs required for a robot to achieve omnidirectional movement. We can take the example of a tendon-driven continuum robot, where three tendons are the minimum number required to achieve omnidirectional steering.

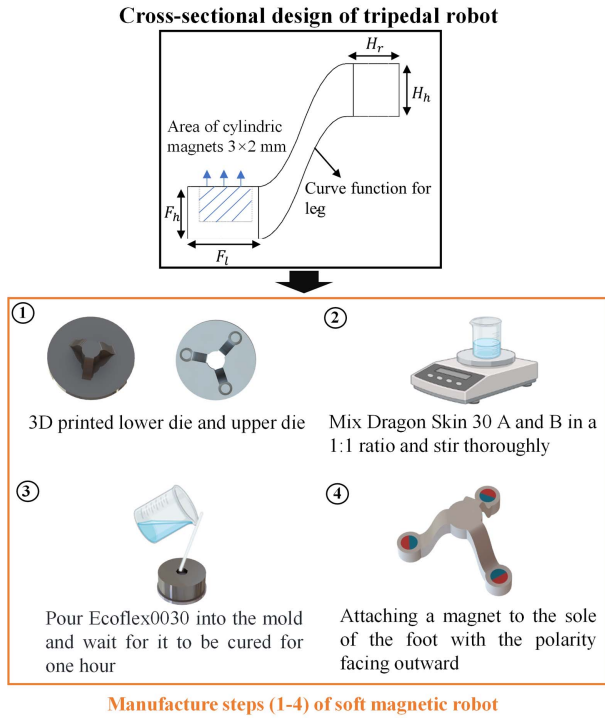


Fig. 2. Illustration of the cross-sectional diagram of a one-third soft magnetic robot. The manufacturing steps of the soft magnetic robot (1-4).

In the gastrointestinal tract, we investigated the narrowest diameter ranges for each section in adults: the esophagus (diameter: 20 mm), stomach (pylorus diameter: 13-20 mm), small intestine (diameter: 25 mm), and large intestine (diameter: 48 mm). Therefore, the overall size of the robot should not exceed 2 cm. The robot must perform an upward thrusting motion to insert the microneedle. Then, in the third step, we can determine the structure of the magnetic soft robot. Therefore, the robot's feet need to be connected to a curved leg design, allowing the leg to protrude outward when subjected to magnetic torque. The fourth step is to design the magnetic arrangement of the robot. To generate such magnetic torque, it is necessary for the magnets on the robot's feet to have their polarities facing outward. Additionally, considering the effectiveness of tissue penetration, the robot needs to have a certain degree of payload capacity. Based on the literature research on the insertion force of microneedle [11], [24], [25], a payload of 20 g has been selected for our design.

Fig. 2 illustrates the specific manufacturing process: the first step involves using 3D printing to produce the upper and lower molds, with the upper mold having three cylindrical cavities for permanent magnets. Afterward, Dragon Skin 30 A:B mixture is prepared by combining equal weights of both components (A and B) and thoroughly stirring them together. In the third step, the mixed Dragon Skin 30 solution is poured into the molds. Due to its viscous nature, it is necessary to pour the solution in batches gradually to prevent the formation of air bubbles. Finally, the magnets are then affixed onto the pre-designed cavities, ensuring that their polarity aligns with the normal direction of each foot.

TABLE I
PARAMETERS OF THE ROBOT SIZE

Curve function for leg (mm)	H_h	H_r	F_h	F_l	Overall height	Overall diameter
$0.56 \times x^2$ ($x = 0 - 2.5$)	2 mm	2 mm	3 mm	4 mm	10 mm	24 mm

The key parameters of the robot size are listed in Table I. The H_h and H_r represent the height and radius of the robot head. The F_h and F_l represent the robot foot's height and length, respectively. For the design of robot feet, which are the actuated components, it is necessary to adhere to commonly used specifications for cylindrical permanent magnets. In this letter, we have selected neodymium iron boron (NdFeB) magnets with a diameter of 3 mm and a height of 2 mm. The dimension design incorporates a 1 mm clearance space. Regarding the design of the robot legs, the primary consideration is to generate sufficient bending when performing a simple up-and-down motion. In addition, it is also necessary to consider the connection between the foot and the head and ensure that the overall diameter of the robot is limited within the range of 2 cm to 3 cm. Therefore, we choose a quadratic function to generate sufficient bending and adjust the parameters of the quadratic function based on the overall height and diameter of the robot. The design of the robot head size only needs to consider its ability to accommodate functional payloads (such as micro-needles, medication, markers, etc.) within the gastrointestinal tract. The weight of the magnetic soft robot is 0.71 g.

III. EXPERIMENT SETUP

Trajectory record of three motion modalities: The experimental setup shown in Fig. 3(a) includes a host computer, signal generator, power amplifier, camera, and a 3D Helmholtz coil system. First, calibrate the unit (1 V) voltage (DC) in the signal generator to adjust the power amplifier knobs so that they correspond to the 8 V, 8 V, and 6 V of the X, Y, and Z coil, respectively. This calibration aims to limit the real voltage in the power amplifier to 20 V, 20 V, and 15 V when the maximum amplitude of the voltage is set to 5 V in the signal generator. The uniform area range of the coil system (with an error within 2%) is 84 mm × 58 mm × 37 mm. The main experimental area will be this range. Then, programs will be pre-written in the host computer so that signals can be automatically controlled and position data can be collected during the experiment. A square Aruco marker of 1 cm will be attached to the robot's head so the camera can record its trajectory while moving within the coil. The frequency modulation range is from 0.1 to 1 Hz, with an interval of 0.1 Hz.

Force measurement of functional modalities (leg raising): The 6-axis force sensor (OPTOFORCE OMD-10-SE-10 N) will be integrated into a three-axis moving slide table. Then, the three-axis platform is manipulated to position the force sensor at its end at the center of the Helmholtz coil and then gradually move it to a location 12.5 mm above the base. The appropriate distance (12.5 mm) is determined based on the height of the robot with the attached microneedle patch (Fig. 3(b)).

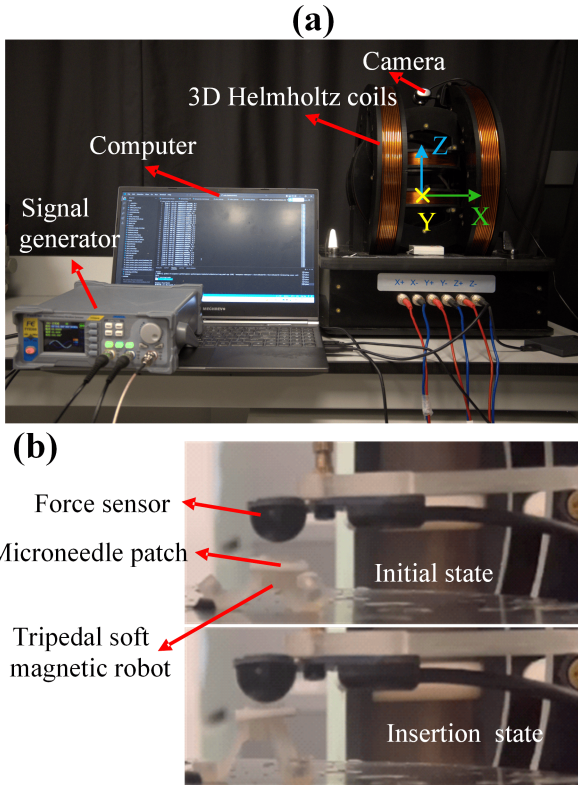


Fig. 3. Experiment setup of soft magnetic robot motion modalities generation. (a) Basic setup for trajectory recording and periodic time recording. (b) The setup is an illustration of the leg-raising modality and force record.

IV. ANALYSIS OF MOTION MODALITY

Initially, a model is constructed to represent the external magnetic field responsible for actuating the robotic mechanism using the 3D Helmholtz coils (PS-3HM376, Hu Nan Pai Sheng Elegance Technology CO., LTD). After calibration, a correlation is established between the current output of the power amplifier and the resultant magnetic flux density:

$$\begin{bmatrix} B_x \\ B_y \\ B_z \end{bmatrix} = \begin{bmatrix} 0.709I_x \\ 0.744I_y \\ 1.606I_z \end{bmatrix} \quad (1)$$

where the B_x , B_y , B_z represents the magnetic flux density (unit: mT) in corresponding XYZ workspace, and I_x , I_y , I_z are current in XYZ coils. Subsequently, an analysis is conducted to evaluate the torque exerted on the permanent magnets, which are integrated into the feet of the robot, in the presence of an externally applied uniform magnetic field. The torque formula is:

$$\tau = \mathbf{m} \times \mathbf{B} \quad (2)$$

where the τ is torque, \mathbf{m} is the magnetic moment, \mathbf{B} is the external magnetic field. Then we can expand (2) in XYZ

workspace as:

$$\begin{bmatrix} \tau_x \\ \tau_y \\ \tau_z \end{bmatrix} = \begin{bmatrix} 0 & -m_z & m_y \\ m_z & 0 & -m_x \\ -m_y & m_x & 0 \end{bmatrix} \begin{bmatrix} B_x \\ B_y \\ B_z \end{bmatrix} \quad (3)$$

We note that for permanent magnets, the magnetic moment can be expressed as:

$$\mathbf{m} = \frac{1}{\mu_0} B_r V \quad (4)$$

where $\mu_0 = 4\pi \times 10^{-7} \frac{N}{A^2}$ is vacuum permeability, $B_r = 1.45$ T is the residual magnetism for NdFeB permanent magnet (N52), $V = \pi r^2 \cdot h = 14.14 \text{ mm}^3$ is the volume of magnet. Then, the magnetic moment of magnets in the foot is 0.0163 Am . Based on (1), (3), (4), we calculate the torques generated by the magnetic field exerted on the robot. We denote the τ_{px} , τ_{py} , and τ_{pz} as torques of posterior foot in XYZ direction, and τ_{px} , τ_{py} , τ_{pz} as torques of anterior foot in XYZ direction.

Butterfly crawling motion: As a tripodal robot, to establish a forward gait (with the positive x direction as an example), it is necessary to utilize the magnetic field in the x direction to direct the two legs that are not parallel to B_x towards the positive direction. However, due to the constraints imposed by material rigidity and the upper bound of the magnetic field force that can be applied, the direct application of a magnetic field in the x direction in an upright initial state would not be effective. Hence, we have devised a configuration that is more conducive to producing an x deflection. Such configuration refers to the robot squatting to its lowest position. Compared to the initial state ($t=0$ s), there is no friction between the robot's feet and the ground. The suspended foot is simultaneously subjected to a torque (τ_y) generated by B_x . As the robot's legs make contact with the coil base, a mechanical structure resembling a cantilever beam is formed. Based on the aforementioned analysis, our design objectives are as follows: 1. The robot must be able to complete the transition from a squatting position to its original state, facilitated by a sine signal with an offset; 2. During the squatting process, the magnetic field in the positive x direction must coincide with this process. The peaks of both signals should either coincide or be in close proximity, with the specific value determined by experimental results. This can be achieved through the generation of a sine signal that exhibits a phase difference from the squatting action signal. The expressions of two signals are:

$$I_{x(y)} = A_{x(y)} \sin(2\pi ft - \phi_{x(y)}) \quad (5)$$

$$I_z = A_z \sin(2\pi ft) - \frac{A_z}{2} \quad (6)$$

We have noted the following observations: 1. Both signals are capable of frequency modulation and must remain consistent with one another; 2. The phase difference $\phi_{x(y)}$ primarily determines the direction of movement along the x or y axis, either in the positive or negative direction (i.e., whether $+B_x$ coincides with the signal prior to squatting or $-B_x$). 3. When deciding on the direction of movement, the value of the phase difference can also influence the stride length.

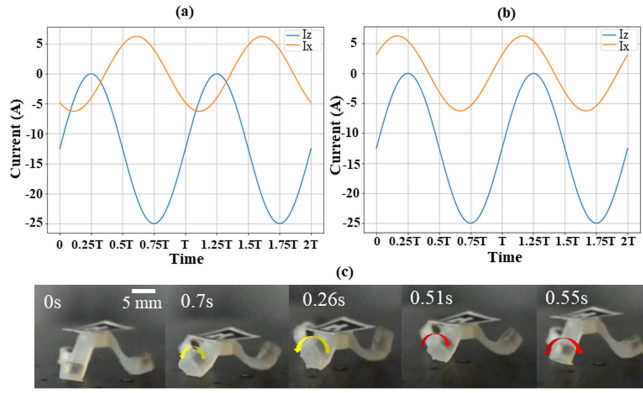


Fig. 4. (a) Control signals that allow the robot to move in the $+B_x(y)$ direction ($\phi_{x(y)} = 130^\circ$, $A_{x(y)} = 6.25$ A, $A_z = 12.5$ A). (b) Control signals that allow the robot to move in the $-B_x(y)$ direction ($\phi_{x(y)} = 330^\circ$, $A_{x(y)} = 6.25$ A, $A_z = 12.5$ A). (c) The snapshot of the side perspective of the robotic motion, captured when the frequency parameter is set to 0.5 Hz.

In Fig. 4(c), observations from the experimental trials indicate that within the time interval of 0.7 s to 0.26 s, the robot moves downward with torque exerted on posterior feet. The torque has the opposite influence on moving in the desired direction, but this effect can be eliminated by positive torque (will be shown in Section V). At the squat state ($t = 0.26$ s), the torques are $\tau_{px} = -0.283$ mN · m, $\tau_{py} = -0.173$ mN · m, $\tau_{pz} = -0.049$ mN · m, $\tau_{az} = -0.122$ mN · m. From 0.51 s to 0.55 s, the posterior pair of feet exhibits a noticeable response to the influence of B_x , resulting in a forward progression through incremental steps. Meanwhile, the robot recovered its initial configuration actuated by B_z . At $t = 0.55$ s, the torques are $\tau_{px} = -0.283$ mN · m, $\tau_{py} = -0.173$ mN · m, $\tau_{pz} = -0.049$ mN · m, $\tau_{az} = -0.122$ mN · m.

Scorpion crawling motion: The butterfly crawling motion modality exhibited incremental steps, rendering it suitable for traversal across smooth and level surfaces such as the gastric fundus and esophageal tract. However, this modality proved inadequate when navigating irregular terrains, impeding mobility. Consequently, an alternative moving modality was devised, emulating the ambulatory characteristics of a scorpion. This involved elevating the posterior leg to facilitate a forward tilt of the robot body, while the anterior legs executed a coordinated, alternating movement. Consequently, the initial phase involves the formation of a morphological configuration resembling a raising tail scorpion. At the initial state, the torques exerted on the robot are $\tau_{py} = 0.173$ mN · m, $\tau_{ax} = 0.092$ mN · m, $\tau_{ay} = -0.062$ mN · m, $\tau_{az} = -0.122$ mN · m. Taking into account the previously mentioned squatting position, it is possible to generate a mechanical model analogous to a cantilever beam. In this model, the torque exerted on the posterior legs can increase the lever effect. Assuming that the robot is intended to move in the positive x direction, a DC current can be designed in the downward z direction to facilitate the completion of the squatting motion by the robot. Subsequently, the tail-lifting motion can be accomplished by applying torque in the y direction, generated by B_x . Then, a sinusoidal signal is employed to generate torque in the x direction, facilitating the alternate

TABLE II
PARAMETERS FOR CONTROL SIGNALS IN SCORPION CRAWLING MOTION

Moving direction	A _x	A _y	A _z	offset
X+	-15 A	12.5 A	-5 A	±2.5 A
X-	15 A	12.5 A	-5 A	±2.5 A



Fig. 5. When $f = 0.5$ Hz, the top and side views of the robot in scorpion crawling modality.

movement of the two front legs. Consequently, the control signal can be represented as follows:

$$I_x = A_x \quad (7)$$

$$I_y = A_y \sin(2\pi ft) + C_y \quad (8)$$

$$I_z = A_z \quad (9)$$

where C_y is the offset current. It is noted that when the robot is moving unbalanced, the original symmetry signal of I_y can fail to move the robot in the desired direction. Then, offset current can be used to re-balance the robot. The amplitude and offset are determined by the experiment, and Table II gives the parameters. If we want to move along the y direction, signals of I_x and I_y can be swapped. In Fig. 5, the decomposition of scorpion crawling is shown. At $t = 1.07$ s, torque required to move the anterior foot is $\tau_{az} = 0.122$ mN · m.

Rolling motion: In designing the rolling motion, the scorpion tail-lifting motion is taken as a basis. By increasing the torque generated by B_x , it is possible to cause the robot to roll over onto its back. Subsequently, once the robot has flipped over, it is necessary to evaluate whether the torque generated by B_x is in a certain range to sustain the robot's forward rolling motion and enable it to return to its initial configuration. Based on the aforementioned analysis, the first step in designing the signal involves experimentally determining the amplitude of I_x . Subsequently, an analysis is conducted to ascertain whether the phase difference between the sinusoidal signal and the vertical motion signal in the z direction is sufficient to facilitate the completion of the remaining rolling motion. We adopted two control signals ((5) and (6)) in the butterfly crawling motion, but the specific parameters (($\phi_{x(y)} = 130^\circ$, $A_{x(y)} = 12.5$, $A_z = 12.5$)) were determined through experimental trials.

In Fig. 6, the process of rolling can be subdivided into five distinct stages, denoted as p1 through p5. During the first stage (p1), the hind legs are elevated by a torque originating from (- B_x) while the squatting posture is maintained. In the second stage (p2), following the completion of a lateral flip, the magnetic field along the z -axis gradually diminishes to zero, resulting in a transient callback phase experienced by the robot. In the third stage (p3), the magnetic field along the z -axis begins to increase, and there remains a residual torque $-B_x$, culminating in a successful flipover. The torques exerted on the robot are

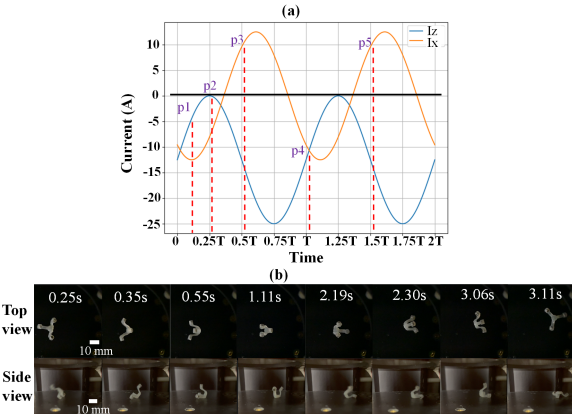


Fig. 6. (a) Control signals of current in X and Z direction. (b) The snapshot of the top view and side view of the rolling motion, captured when the frequency is set to 0.5 Hz.

$\tau_{py} = 0.061 \text{ mN} \cdot \text{m}$, $\tau_{pz} = 0.053 \text{ mN} \cdot \text{m}$, $\tau_{az} = -0.074 \text{ mN} \cdot \text{m}$. During the fourth stage (p4), the robot remains in a flipped-over state for a duration due to the presence of an opposing torque from $+Bx$. Concurrently, a 180° rotation is executed, setting the stage for the fifth phase (p5), where the robot returns to its initial configuration. In the final stage (p5), the robot is once again subjected to the influence of $-Bx$, resulting in the generation of clockwise torque in both the front and hind legs, culminating in the completion of the recovery process. The torques required to flip over the robot again is computed to be $\tau_{py} = -0.096 \text{ mN} \cdot \text{m}$, $\tau_{ax} = -0.260 \text{ mN} \cdot \text{m}$, $\tau_{az} = -0.076 \text{ mN} \cdot \text{m}$.

V. RESULTS

In the preceding section, an analysis was conducted on three distinct modes of motion. This analysis encompassed the identification of control signals capable of executing the corresponding actions, as well as the determination of critical parameters, including phase, offset, and amplitude. Consequently, in this section, we will examine the frequency parameter, building upon the control established by the previous signals. Through experimentation, we will observe the characteristics of motion trajectories under varying frequency conditions. Furthermore, under varying frequency modulations, given that the distance traversed by the robot in rolling mode remains constant, our primary focus will be on recording the duration of a complete rolling cycle. Finally, an analysis will be conducted on the performance of functional modes. As outlined in the introduction, functional modes are frequently employed for procedures such as biopsy and puncture, which necessitate vertical movement. As such, our chosen metric for measurement is the magnitude of the force exerted under the control of varying signals.

Results of butterfly crawling and scorpion scrawling motion: In Fig. 7(a), we used the control signal for butterfly crawling motion in different frequencies (from 0.1 Hz to 1.0 Hz). An Aruco marker has been affixed to the top of the robot, serving to record displacement in the x-direction. At each frequency, ten sets of data were sampled. Our observations indicate that a wavy trajectory is exhibited at each frequency. Upon examination of

the wavy trajectory, it was determined that the results were consistent with our previous torque analysis. Specifically, due to the presence of a symmetrical sine signal, an initial stage characterized by backward torque (corresponding to the section from the initial point to the trough in the waveform) must be traversed, followed by a stage characterized by forward torque (from the trough to the peak). The presence of a phase difference results in a greater distance traveled during the forward stage as compared to the backward adjustment distance, thereby enabling the robot to maintain overall forward progress. In addition, we obtained the speed at each frequency by fitting the trajectory, as shown in Fig. 8. We applied the linear fitting function to butterfly crawl speed and obtained $v = 5.82f - 0.70$, where the R-squared value is 0.98. As an example, for a frequency of 0.5 Hz, we calculated a step length of 4.13 mm for one crawling cycle.

For the scorpion crawling motion, we also sampled ten sets of data at each frequency. In Fig. 7(b), we can see that it is also a wavy trajectory, but unlike the butterfly crawling motion, when the first front leg moves, the trajectory shows a slight backward movement. When the second front leg moves, it is the stage of moving straight up on the line to be level with the leg that moved first. In the actuation experiment, if the tail of the robot is not aligned with the center line, the robot can fail to crawl like a scorpion after a few steps. Then, we decide to apply an asymmetric sine wave control signal ($Ay = 10$ and offset to be ± 2.5) in the y direction to generate scorpion crawl motion. This is to prevent the robot's foot from crossing the center line. Meanwhile, for 0.5 Hz, we found it is the only frequency that can apply balanced magnetic torque. We believe that the alternating step rate generated by 0.5 Hz is optimal for the robot to maintain balance. Based on Fig. 8, 0.1-0.4 Hz can be clustered into one category. After linear fitting, the velocity increment within this range is 6.21 mm/s per Hz. For the 0.6-1.0 Hz range, we used linear fitting and obtained a speed increment of 9.35 mm/s per Hz with the corresponding R-squared to be 0.9166. For 0.5 Hz denoted as (s) in Figs. 7(b) and 8, we generated the larger amplitude in the y direction can improve the velocity to 6.14 mm/s, which surpasses the velocities at 0.6 Hz and 0.7 Hz and is at the same magnitude as 0.8 Hz. Then, when $f=0.5$ Hz, we computed the stride of crawl mode to be 9.90 mm.

Results of rolling motion: In Fig. 7(c), the time (unit in ms) required to complete a rolling and the corresponding different frequencies are recorded. It appears to be an exponential decay curve. By applying the exponential fitting function, we obtain:

$$T = 15551.69e^{-4.86f} \quad (10)$$

The related r-squared value is 0.92. In addition, for better fitting results, we also used a power function to fit the data. The power function is determined to be:

$$T = 827.17f^{-1.09} \quad (11)$$

The related r-squared value is 1.0, which shows a better-fitting result than the exponential function.

Results of insertion force under different control signals: For Microneedle, the efficiency of these functions can be evaluated by the magnitude of the insertion force. The magnitude of

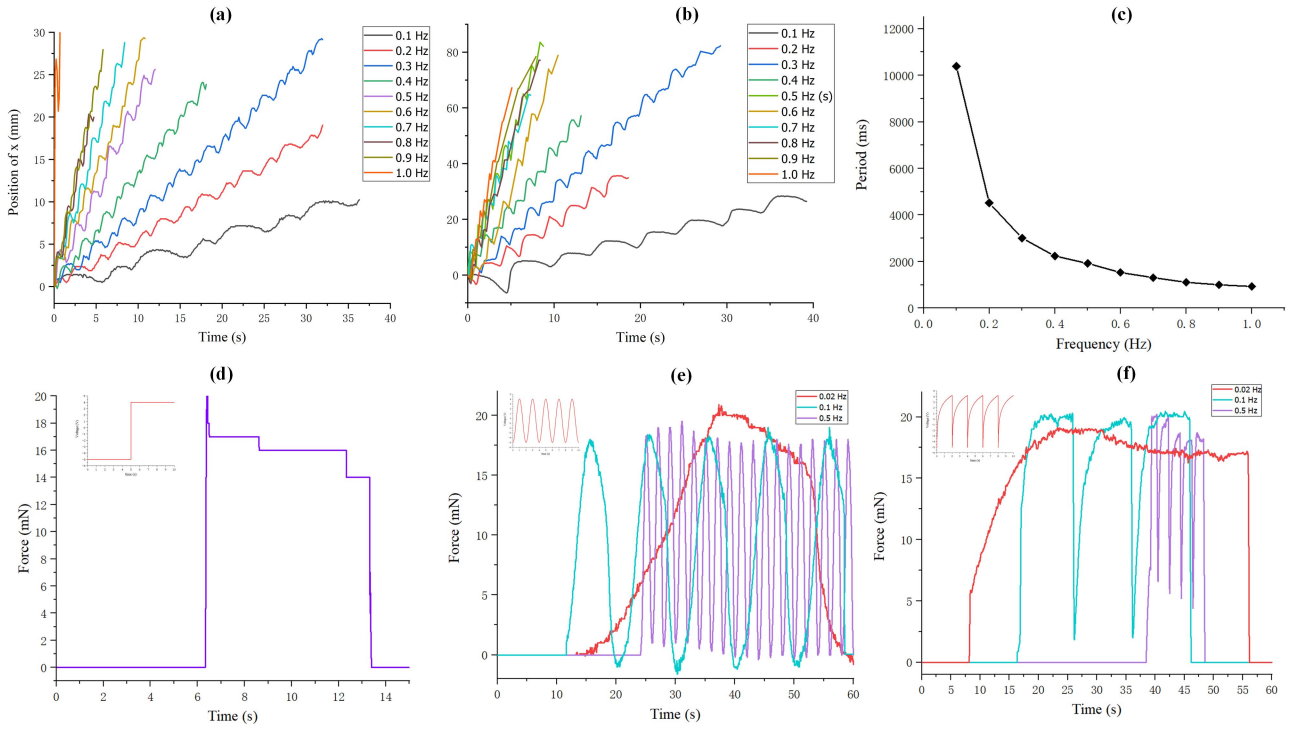


Fig. 7. (a) Trajectory along the $x+$ direction of butterfly crawling motion is recorded. (0.1 to 1.0 Hz) (b) The trajectory along the $x+$ direction of the scorpion crawling motion is recorded. (0.1 to 1.0 Hz) (c) The period required to complete a full roll (0.1-1.0 Hz). (d) Force profile under step signal ($-6.25\text{-}6.25$ V). (e) Force profiles under actuation of cosine signals ($-6.25\text{-}6.25$ V) at different frequencies (0.02 Hz, 0.1 Hz, 0.5 Hz). (f) Force profiles under actuation of inverse exponential signals ($-6.25\text{-}6.25$ V) at different frequencies (0.02 Hz, 0.1 Hz, 0.5 Hz).

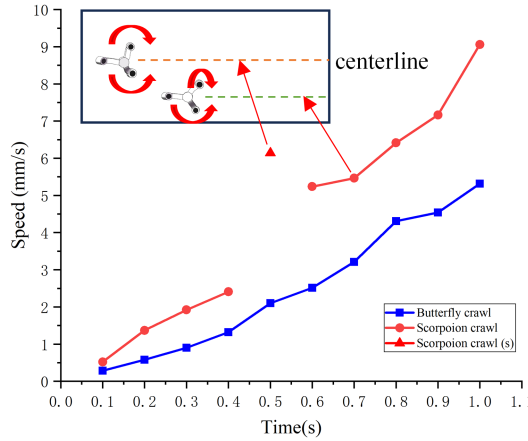


Fig. 8. Speed (mm/s) of butterfly crawling motion and scorpion crawling motion at different frequencies.

the contact and insertion forces during microneedle insertion is influenced by several factors, including the speed of the robot's movement. To optimize these forces, we have designed and implemented various control signals, including step, cosine (with frequencies of 0.02 Hz, 0.1 Hz, and 0.5 Hz), and inverse exponential signals (with frequencies of 0.02 Hz, 0.1 Hz, and 0.5 Hz). The maximum force exerted by the robot-mounted microneedle upon contact with the force sensor and the average force after stabilization are recorded. As shown in Fig. 7(d), the

step signal initially rises to a peak value before quickly falling back to a steady state. Although the steady state appears in two segments in the image, the error is within 1 mN, which falls within the measurement error of the sensor's noise range. As shown in Fig. 7, the force curves correspond to the cosine signals at 0.02 Hz, 0.1 Hz, and 0.5 Hz. The force curves at 0.1 Hz and 0.02 Hz exhibit higher stability than those at 0.5 Hz. This observation also applies to the inverse exponential signals depicted in Fig. 7(f). The signal at 0.5 Hz ($\sigma_{0.5 \text{ Hz}} = 4.7$) has a higher variance in peak values than 0.1 Hz ($\sigma_{0.1 \text{ Hz}} = 0.33$) and 0.02 Hz ($\sigma_{0.02 \text{ Hz}} = 0.15$). Furthermore, when comparing the signals at 0.1 Hz and 0.02 Hz, it can be observed that the signal at 0.1 Hz is better able to recover the waveform of the original control signal. In contrast, the signal at 0.02 Hz exhibits certain distortion after surpassing the peak force value.

Ten sets of samples were taken for each signal, and the average peak force and stable force were calculated and displayed in Table III. Contrary to expectations, the peak value of the step signal did not surpass those of the cosine and inverse exponential signals. With regards to the force during the stable stage, the inverse exponential wave at 0.1 Hz (20 mN) was observed to be higher than both the step signal and the inverse exponential signals at other frequencies.

Illustration of moving in ex vivo swine stomach: As demonstrated in the **supplementary video**, the robot, under the control of various signals, navigated the complex environment of an *ex vivo* swine stomach. By employing a range of previously

TABLE III
CONTACT FORCE UNDER DIFFERENT TYPES OF SIGNALS

Type of signal	Average peak force (mN)	Average steady force (mN)
Step signal	20	16
0.5 Hz (cosine signal)	19	N/A
0.1 Hz (cosine signal)	19	N/A
0.02 Hz (cosine signal)	21	N/A
0.5 Hz (Inverse exponential signal)	21.6	19
0.1 Hz (Inverse exponential signal)	21	20
0.02 Hz (Inverse exponential signal)	19.3	16.5

adopted motion modalities, the robot successfully overcomes challenging terrain.

Illustration of moving in the liquid environment: As demonstrated in the **supplementary video**, the robot was placed at the bottom of a plastic bottle, submerged in water. The robot is still capable of performing both butterfly crawling and scorpion crawling movements. Additionally, due to the buoyancy effect, the required magnetic field intensity has also reduced to one-third of its previous value. The robot was also placed inside a stomach model filled with water to test its ability to perform butterfly crawling.

VI. CONCLUSION AND FUTURE WORK

In conclusion, this work presents the design and development of a tripodal soft magnetic drive robot, intended for use within the digestive tract. The robot can exhibit a diverse range of motion modalities, including butterfly crawling, scorpion crawling, and rolling, which are generated through an external uniform magnetic field. Despite the butterfly crawling motion exhibiting comparatively weaker performance in terms of speed, stride length, and vertical traversal capabilities, its unique advantage lies in its omnidirectional mobility. It is important to note that all motion modalities of the robot can be frequency-modulated. Different frequencies can result in distinct patterns in terms of speed and period. When it comes to the functional modality of leg-raising, the force profile stands out as the key determinant of its effectiveness. Consequently, we conducted a comparative analysis of three control signals. Considering the metrics of stability and maximum impact force, the cosine signal and its corresponding frequency emerged as the optimal choice, following a comprehensive and balanced evaluation. The developed robot was tested in an *ex vivo* stomach and demonstrated its ability to navigate different terrains using various moving modalities. This work represents a significant step towards developing multi-functional magnetic-driven soft robots for noninvasive diagnosis and treatment within the medical field.

REFERENCES

- [1] Y. Wang, J. Shen, S. Handschuh-Wang, M. Qiu, S. Du, and B. Wang, "Microrobots for targeted delivery and therapy in digestive system," *ACS Nano*, vol. 17, no. 1, pp. 27–50, 2022.
- [2] F. Zhang et al., "Gastrointestinal tract drug delivery using algae motors embedded in a degradable capsule," *Sci. Robot.*, vol. 7, no. 70, 2022, Art. no. eab04160.
- [3] J. Sun, H. Tan, S. Lan, F. Peng, and Y. Tu, "Progress on the fabrication strategies of self-propelled micro/nanomotors," *JCIS Open*, vol. 2, 2021, Art. no. 100011.
- [4] Y. Kim and X. Zhao, "Magnetic soft materials and robots," *Chem. Rev.*, vol. 122, no. 5, pp. 5317–5364, 2022.
- [5] H. Gu et al., "Magnetic cilia carpets with programmable metachronal waves," *Nature Commun.*, vol. 11, no. 1, 2020, Art. no. 2637.
- [6] W. Hu, G. Z. Lum, M. Mastrangeli, and M. Sitti, "Small-scale soft-bodied robot with multimodal locomotion," *Nature*, vol. 554, no. 7690, pp. 81–85, 2018.
- [7] Y. Wu, X. Dong, J.-K. Kim, C. Wang, and M. Sitti, "Wireless soft millirobots for climbing three-dimensional surfaces in confined spaces," *Sci. Adv.*, vol. 8, no. 21, 2022, Art. no. eabn3431.
- [8] H. Lu et al., "A bioinspired multilegged soft millirobot that functions in both dry and wet conditions," *Nature Commun.*, vol. 9, no. 1, 2018, Art. no. 3944.
- [9] C. Huang, T. Xu, and X. Wu, "Leader–follower formation control of magnetically actuated millirobots for automatic navigation," *IEEE/ASME Trans. Mechatronics*, early access, Aug. 10, 2023, doi: 10.1109/TMECH.2023.3300010.
- [10] T. Xu, C. Huang, Z. Lai, and X. Wu, "Independent control strategy of multiple magnetic flexible millirobots for position control and path following," *IEEE Trans. Robot.*, vol. 38, no. 5, pp. 2875–2887, Oct. 2022.
- [11] J. Lee, H. Lee, S.-H. Kwon, and S. Park, "Active delivery of multi-layer drug-loaded microneedle patches using magnetically driven capsule," *Med. Eng. Phys.*, vol. 85, pp. 87–96, 2020.
- [12] W. Chen, J. Sui, and C. Wang, "Magnetically actuated capsule robots: A review," *IEEE Access*, vol. 10, pp. 88398–88420, 2022.
- [13] S. Song et al., "Integrated design and decoupled control of anchoring and drug release for wireless capsule robots," *IEEE/ASME Trans. Mechatronics*, vol. 27, no. 5, pp. 2897–2907, Oct. 2022.
- [14] J. Miao and S. Sun, "Design, actuation, and functionalization of untethered soft magnetic robots with life-like motions: A review," 2023, arXiv:2305.17734.
- [15] S.S. Srinivasan et al., "RoboCap: Robotic mucus-clearing capsule for enhanced drug delivery in the gastrointestinal tract," *Sci. Robot.*, vol. 7, no. 70, 2022, Art. no. eabp9066.
- [16] C. Huang, Z. Lai, X. Wu, and T. Xu, "Multimodal locomotion and cargo transportation of magnetically actuated quadruped soft microrobots," *Cyborg Bionic Syst.*, vol. 2022, 2022, Art. no. 0004.
- [17] Y. Wang, X. Du, H. Zhang, Q. Zou, J. Law, and J. Yu, "Amphibious miniature soft jumping robot with on-demand in-flight maneuver," *Adv. Sci.*, vol. 10, 2023, Art. no. 2207493.
- [18] H. Li, G. Go, S. Y. Ko, J.-O. Park, and S. Park, "Magnetic actuated pH-responsive hydrogel-based soft micro-robot for targeted drug delivery," *Smart Mater. Structures*, vol. 25, no. 2, 2016, Art. no. 027001.
- [19] Y. Kim, H. Yuk, R. Zhao, S. A. Chester, and X. Zhao, "Printing ferromagnetic domains for untethered fast-transforming soft materials," *Nature*, vol. 558, no. 7709, pp. 274–279, 2018.
- [20] J. Zhang et al., "Voxelated three-dimensional miniature magnetic soft machines via multimaterial heterogeneous assembly," *Sci. Robot.*, vol. 6, no. 53, 2021, Art. no. eabf0112.
- [21] S. Yuan et al., "Versatile motion generation of magnetic origami spring robots in the uniform magnetic field," *IEEE Robot. Automat. Lett.*, vol. 7, no. 4, pp. 10486–10493, Oct. 2022.
- [22] C. J. Cai, B. S. Yeow, H. Huang, C. Laschi, and H. Ren, "Magnetically actuated lamina emergent mechanism for bimodal crawling and flipping locomotion," *IEEE/ASME Trans. Mechatronics*, early access, Aug. 08, 2023, doi: 10.1109/TMECH.2023.3297722.
- [23] C. J. Cai et al., "Diversified and untethered motion generation via crease patterning from magnetically actuated caterpillar-inspired origami robot," *IEEE/ASME Trans. Mechatronics*, vol. 26, no. 3, pp. 1678–1688, Jun. 2021.
- [24] A. Abramson et al., "A luminal unfolding microneedle injector for oral delivery of macromolecules," *Nature Med.*, vol. 25, no. 10, pp. 1512–1518, 2019.
- [25] S. Y. Yang et al., "A bio-inspired swellable microneedle adhesive for mechanical interlocking with tissue," *Nature Commun.*, vol. 4, no. 1, 2013, Art. no. 1702.